A numerical efficiency study on the active vibration control for a FGPM beam

Jonas Maruani, Isabelle Bruant, Frédéric Pablo, Laurent Gallimard

▶ **To cite this version:**

HAL Id: hal-01678026
https://hal.parisnanterre.fr/hal-01678026

A numerical efficiency study on the active vibration control for a FGPM beam

Jonas Maruani[*], Isabelle Bruant, Frédéric Pablo, Laurent Gallimard

Laboratoire Énergétique, Mécanique, Électromagnétisme, EA 4416, Université Paris Nanterre, 50 rue de Sèvres 92410 Ville d'Avray, France

1. Introduction

In the recent years, a great deal of research on active vibration control has been carried out for light-weight smart structures such as aerospace, nuclear and automotive structural applications.

Several active vibration control strategies have been successfully implemented to reduce vibrations of beams, plates and shells, using distributed piezoelectric patches. Indeed, piezoelectric materials have specific characteristics, like light weight, high strength, easily shaped and good frequency response, that make them attractive actuators and sensors.

Classical piezoelectric smart structures are multilayered composites with piezoelectric patches adhesively bounded to the host structure, either at its surfaces or inside it [1].

These conventional smart structures suffer high stresses concentration near interlayer surfaces because of abrupt changes in electro-mechanical properties. Moreover, the adhesive layer may crack at low temperatures and creep or pell at high temperature [2], which can lead to severe deteriorations of the interlayer bounding strength and response performance.

The functionally graded piezoelectric material (FGPM), a new class of the well known functionally graded material (FGM) [3], have attracted much attention these last years. They are designed to achieve a functional performance with mechanical and piezoelectric properties that gradually evolve along one or several directions. This continuity allows to avoid the aforementioned disadvantages of classical piezoelectric smart structures. This way, the substitution of classical piezoelectric smart structure by a FGPM structure seems to be an attractive choice for active vibration control.

Most of the published work on FGPM deals with numerical simulations. It is mainly focused on static bending, free vibration analysis and dynamic response of FGPM structures under different loading conditions. These FGPM are generally made of a mixture of two piezoelectric materials. Several authors studied FGPM beams or plates under thermo-electro-mechanical loads: static analysis have been performed in [4–7] and modal analysis in [8–12]. The geometrically non linear transient thermo-elastic response of FGM beam integrated with a pair of FGPM sensors has been investigated in [13].

Regarding the active vibration control using functionally graded material, we can find in literature papers dealing with active vibration control of FGM equipped with piezoelectric patches [14–24].

Since the active vibration control with FGPM is a relatively new topic, very limited works can be found in open literature. Non linear active control of FG beams in thermal environments subjected to blast loads with integrated FGPM sensors and actuators layers was developed in [25]. In [26] and [27] active vibration control using PZT/Pt based FGPM has been performed. In these three papers, sensors and actuators are made of FGPM and are bounded symmetrically on the entire top and bottom faces of the host structure.

The present paper deals with active vibration control of a FGPM beam. The host structure and the piezoelectric sensors and actuators are substituted by a single FGPM structure, which ensures continuity on the

---

[*] Corresponding author.

E-mail address: jonas.maruani@parisnanterre.fr (J. Maruani).

mechanical and piezoelectric properties. This FGPM is made of a mixture between PZT4 and aluminium, such that its composition varies from aluminium at the mid surface to PZT4 at the top and bottom surfaces. Mixing dielectric and conductive materials leads to percolation phenomenon: the FGPM switches from insulating behaviour to a conductive one according to the concentration of conductive particles [28,29]. In order to activate piezoelectric properties for active vibration control, the beam's top and bottom surfaces are covered by a set of electrodes such as a printed wiring in electronics. These particular electrodes' configurations then define the location and dimensions of integrated sensors and actuators (collocated or not). The LQR method used to perform active control, ensures stability for both configurations.

The main originality of this study is the use of:

- a smart structure made out of a single FGPM layer having actuation and sensing capabilities (via electrodes)
- a model including the percolation phenomenon
- several set of sensors/actuators which can be activated via the network of discrete electrodes, according to the external perturbation

The organisation of this paper is as follows. The geometry and FGPM's behaviour laws which depend on z-direction, the volume fraction index k and the percolation threshold V_T are presented in the Section 2. The finite element formulation for FGPM beam is obtained Section 3. In Section 4, the control system for performing the active vibration control is presented. Parametric studies are subsequently conducted in Section 5 to show the effect of the volume fraction index k and the percolation threshold V_T on the static and dynamic response of a FGPM beam. The influence of electrodes' length and location is also investigated. The main conclusions are summarized in Section 6.

2. FGPM Timoshenko beam model

2.1. Geometry

We consider a plane and straight FGPM beam whose dimensions are the length L, the thickness h and the width b. The FGPM is made of a mixture between PZT4 and aluminium (Fig. 1). We consider that the material properties vary continuously across the thickness direction, so that top and bottom surfaces consist of pure PZT4 and the mid surface is composed of pure aluminium.

2.2. Timoshenko piezoelectric beam model

To avoid restriction on the thickness, the Timoshenko beam theory is used. According to Timoshenko beam theory, the displacement field (u_1,u_3) of the FGPM beam reads [30]:

$$\begin{cases} u_1(x,z,t) = u_0(x,t) + z\theta_0(x,t) \\ u_3(x,z,t) = w_0(x,t) \end{cases} \quad (1)$$

where θ_0 is the rotation of the cross-section of the beam about the y axis and (u_0,w_0) are the displacement components in x and z direction
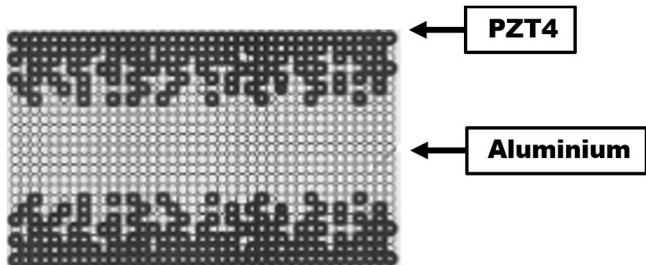
respectively.

The FGPM is further supposed to be polarized along the z axis. Therefore, only the transverse electric field, $E_3(x,z,t)$ will be considered. Thus the three constitutive equations for the FGPM beam are the following:

$$\begin{cases} \sigma_{11}(x,z,t) = Y(z)\varepsilon_{11}(x,z,t) + e_{31}(z)E_3(x,z,t) \\ \sigma_{13}(x,z,t) = G(z)\gamma_{13}(x,z,t) \\ D_3(x,z,t) = e_{31}(z)\varepsilon_{11}(x,z,t) + \epsilon_{33}(z)E_3(x,z,t) \end{cases} \quad (2)$$

where $Y(z),G(z),e_{31}(z),\epsilon_{33}(z)$ are the Young modulus, the shear modulus, the piezoelectric constant and the permittivity constant, respectively, and where:

$$\varepsilon_{11} = \frac{\partial u_1}{\partial x}; \quad \gamma_{13} = \left(\frac{\partial u_1}{\partial z} + \frac{\partial u_3}{\partial x}\right) \quad (3)$$

The electric field is related to electric potential ϕ by:

$$E_3(x,z,t) = -\frac{\partial \phi(x,z,t)}{\partial z} \quad (4)$$

2.3. Material behaviour laws

A mixture between a dielectric and a conductive components, respectively here PZT4 and aluminium, has particular electric properties, when V_m the concentration of the metallic component, reaches the percolation threshold. At this concentration, noted V_T, the composite undergoes a conductive-insulator transition: below V_T, the composite has an insulating behaviour and above V_T, the composite has a conductive behaviour [29].

The percolation occurs when there are enough metallic particles to form a conductive path into the mixture. The percolation threshold is usually obtained through dedicated experimental measures and it depends on the microstructure of the mixture (shape and size of materials' particles [29]). Based on models of percolation theory [28] and experimental studies [31,32] we shall assume that V_T varies in the range [0.1,0.3].

Since the FGPM is assumed to be symmetrically distributed with respect to the Al mid surface, three regions can be identified: a conductive, Al-rich region centred about the mid surface where the percolation has occurred and two outer insulating regions in which the concentration of metallic particles is below the percolation threshold (Fig. 2).

2.3.1. Properties homogenisation

The addition of metal particles into a dielectric matrix increases the composite's permittivity significantly. Effective medium theories like Maxwell-Garnett theory or Bruggeman theory can be used to estimate the permittivity. In this study, particles are dispersed in a continuous ceramic matrix. The effective permittivity ϵ, is thus given by Maxwell-Garnett rule [28]:

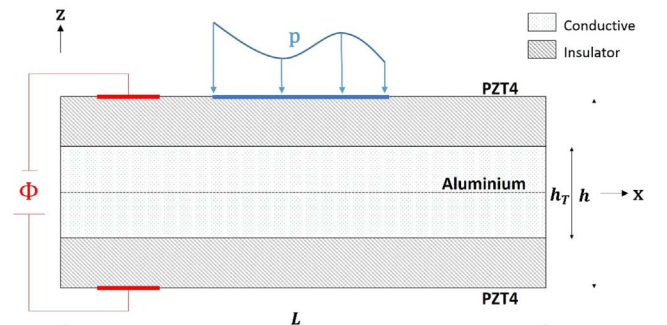Fig. 1. Schematic of the considered PZT4/Al/PZT4 FGPM.

Fig. 2. FGPM beam model.

$$\epsilon(V_m) = \epsilon_p \left(\frac{1 + 2V_m \frac{\epsilon_m - \epsilon_p}{\epsilon_m + 2\epsilon_p}}{1 - V_m \frac{\epsilon_m - \epsilon_p}{\epsilon_m + 2\epsilon_p}} \right) \tag{5}$$

where V_m is the metal volume fraction and p,m subscripts refer to piezoelectric ceramic and metal respectively.

We assume that metal particles can be represented by a dielectric material with strong dielectric losses (ie with a dominant imaginary part), and the ceramic matrix can be represented by a perfect dielectric material (without dielectric losses). In addition at low frequencies, dielectric losses of metal particles tend to infinity. The effective permittivity constant becomes [31,33]:

$$\epsilon(V_m) \simeq \epsilon_p \frac{1 + 2V_m}{1 - V_m}, \quad \epsilon_m \gg \epsilon_p \tag{6}$$

A simple law of homogenisation is used for the Young modulus Y, the density ρ and the piezoelectric constant e_{31}, and can be expressed as [9]:

$$P = (P_m - P_p)V_m + P_p \quad \text{where } P = \{Y, \rho, e_{31}\} \tag{7}$$

2.3.2. Power law distribution

We assume that the volume fraction varies according to a simple power law distribution along the z direction, which can be given as [9]:

$$V_m(z) = \left(1 - \frac{2|z|}{h}\right)^k, \quad z \in \left[\frac{-h}{2}, \frac{h}{2}\right] \tag{8}$$

where k is the non-negative fraction index which may vary from 0 to ∞.

The thickness of the conductive part h_c depends on both the percolation threshold and the fraction index, and can be derived from Eq. (8) by setting $V_m(z = \frac{h_c}{2}) = V_c$ (see Fig. 3):

$$h_c = h\left(1 - V_c^{\frac{1}{k}}\right) \tag{9}$$

As a consequence the Young modulus Y, the density ρ and the piezoelectric constant e_{31} can be represented as (Fig. 4):

$$Y(z) = (Y_m - Y_p)\left(1 - \frac{2|z|}{h}\right)^k + Y_p \quad \frac{-h}{2} \leqslant z \leqslant \frac{h}{2} \tag{10}$$

$$\rho(z) = (\rho_m - \rho_p)\left(1 - \frac{2|z|}{h}\right)^k + \rho_p \quad \frac{-h}{2} \leqslant z \leqslant \frac{h}{2} \tag{11}$$

$$e_{31}(z) = \begin{cases} (e_m - e_p)\left(1 - \frac{2z}{h}\right)^k + e_p & h_c \leqslant z \leqslant \frac{h}{2} \\ 0 & -h_c < z < h_c \\ (e_m - e_p)\left(1 + \frac{2z}{h}\right)^k + e_p & \frac{-h}{2} \leqslant z \leqslant h_c \end{cases} \tag{12}$$

The Poisson's ratio is considered constant in this study.

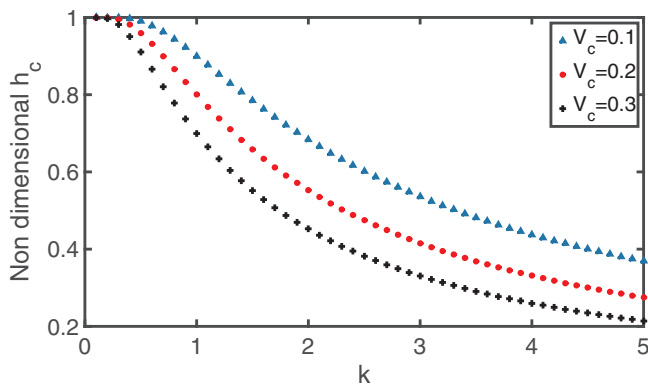Then, substituting Eq. (8) into Eq. (6) the effective permittivity is

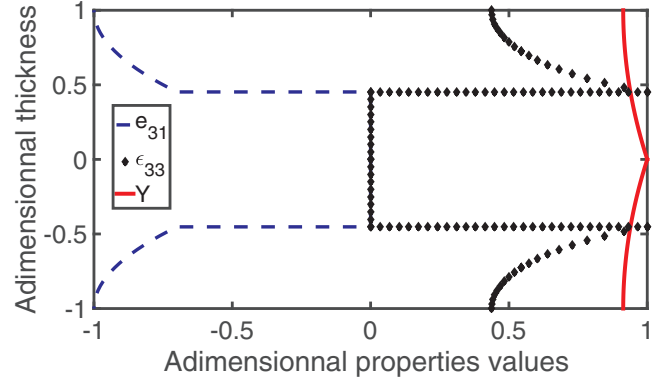**Fig. 3.** Conductive part's non dimensional thickness.

Fig. 4. Effective properties through the thickness for $k = 2$ and $V_c = 0.3$.

given by:

$$\epsilon_{33}(z) = \begin{cases} \epsilon_p \frac{1 + 2\left(1 - \frac{2z}{h}\right)^k}{1 - \left(1 - \frac{2z}{h}\right)^k} & h_c \leqslant z \leqslant \frac{h}{2} \\ 0 & -h_c < z < h_c \\ \epsilon_p \frac{1 + 2\left(1 + \frac{2z}{h}\right)^k}{1 - \left(1 + \frac{2z}{h}\right)^k} & \frac{-h}{2} \leqslant z \leqslant h_c \end{cases} \tag{13}$$

3. Finite element formulation

3.1. Displacement and electric potential approximations

The finite element method is considered to solve the governing equations. A two nodes finite element with a central node is used (Fig. 5).

3.1.1. Displacement approximation

The generalised displacements of the Timoshenko beam model u_0^e, w_0^e, θ_0^e, are approximated in the element by:

$$u_0^e(x,t) = \sum_{j=1}^{2} u_j(t) N_j^l(x)$$

$$w_0^e(x,t) = \sum_{j=1}^{3} w_j(t) N_j^q(x)$$

$$\theta_0^e(x,t) = \sum_{j=1}^{2} \theta_j(t) N_j^l(x) \tag{14}$$

where $N_{j=1,2}^l$ and $N_{j=1,2,3}^q$ are linear and quadratic Lagrange interpolation and u_j, w_j, θ_j are nodal values of u_0^e, w_0^e, θ_0^e respectively. Note that this classical interpolation avoid thickness shear locking, see [30].
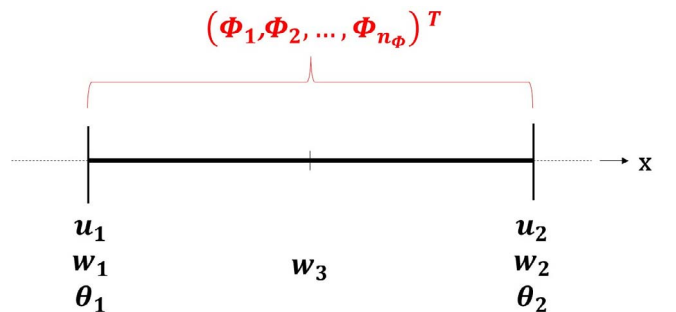

Fig. 5. Reference element's degrees of freedom.

3.1.2. Electric potential approximation

The potential function $\phi(x,z,t)$ is added in order to deal with coupled problems and a layerwise approximation is used in the thickness direction. The main advantage of this choice is to define independently the finite element approximation for the mid place and for the thickness direction.

In order to activate FGPM's piezoelectric properties a portion of beam's top and bottom surfaces are covered by conductive films used as electrodes. Since, the electrodes are equipotential surfaces we consider the electric to be constant per element in x-direction [34].

For a layer l, a quadratic approximation is used for the electric potential through the thickness [35]:

$$\phi_l^e(z) = \sum_{j=1}^{3} \phi_j N_j^q(z) \tag{15}$$

There are three electrical degrees of freedom per numerical layer and a total of $n_\phi = 2n_l + 1$electrical degrees of freedom per element.

3.2. The electro-mechanical system

Variational principles give the following discretized equations [34]:

$$\mathbf{K_{uu}q} + \mathbf{M_{uu}\ddot{q}} + \mathbf{K_{u\phi}\phi} = \mathbf{F} \tag{16}$$

$$\mathbf{K_{\phi\phi}\phi} + \mathbf{K_{\phi u}q} = \mathbf{0} \tag{17}$$

where $\mathbf{M_{uu}}$ is the global mass matrix, $\mathbf{K_{uu}}$ is the global stiffness matrix, $\mathbf{K_{u\phi}}$ and $\mathbf{K_{\phi u}}$ are the global piezoelectric coupling stiffness matrices ($\mathbf{K_{\phi u}} = \mathbf{K_{u\phi}^t}$),$\mathbf{K_{\phi\phi}}$ is the global electric stiffness matrix, $\mathbf{F}$is the applied mechanical force vector, $\mathbf{q}$ is the global nodal displacement vector and ϕ is the global element potential vector.

The potential can be split in two parts, sensor and actuator potentials, and using Eqs. (17) in (16) we have the system [36]:

$$\mathbf{K_{tot}q} + \mathbf{M_{uu}\ddot{q}} = \mathbf{F} + \mathbf{K_a\phi_a} \tag{18}$$

$$\phi_s = -\mathbf{K_{\phi_s\phi_s}^{-1}}(\mathbf{K_{\phi_s u}q} + \mathbf{K_{\phi_s\phi_a}\phi_a}) \tag{19}$$

where indexes s and a represent the sensor and actuator potential respectively, and:

$$\mathbf{K_{tot}} = \mathbf{K_{uu}} + \mathbf{K_{u\phi_s}K_{\phi_s\phi_s}^{-1}K_{\phi_s u}} \tag{20}$$

$$\mathbf{K_a} = \mathbf{K_{u\phi_s}K_{\phi_s\phi_s}^{-1}K_{\phi_s\phi_a}} - \mathbf{K_{u\phi_a}} \tag{21}$$

To perform dynamic analysis we assume a harmonic oscillation with $\mathbf{q} = \mathbf{\Psi}e^{i\omega t}$. Thus, eigenfrequencies ω and the associated modes shapes $\mathbf{\Psi}$ are obtained from the following classical eigenvalue problem::

$$(\mathbf{K_{tot}} - \omega^2\mathbf{M_{uu}})\mathbf{\Psi} = 0 \tag{22}$$

To carry out static analysis, the acceleration vector $\ddot{\mathbf{q}}$ is set to zero and the following system is solved:

$$\mathbf{K_{tot}q} = \mathbf{F} + \mathbf{K_a\phi_a} \tag{23}$$

$$\phi_s = -\mathbf{K_{\phi_s\phi_s}^{-1}}(\mathbf{K_{\phi_s u}q} + \mathbf{K_{\phi_s\phi_a}\phi_a}) \tag{24}$$

4. The control system

To apply active vibration control to dynamic structural problems, the state-space form is useful [37]. This form is based on the displacement's decomposition in the normalized orthogonal structural modal basis.

4.1. The modal analysis

Assuming that contribution of the highest modes is negligible, only the N first modes are considered. Then the displacement can be approximated by:

$$\mathbf{q} = \sum_{n=1}^{N} \mathbf{\Psi_n\alpha_n(t)} = \mathbf{\Psi\alpha} \tag{25}$$

where $\mathbf{\Psi}$ is the modal shape matrix and $\alpha_n(t)$ the nth modal coordinate of the displacement $\mathbf{q}$.

Introducing Eq. (25) into Eqs. (18) and (19) and recalling the orthogonality of eigenmodes yields:

$$\ddot{\alpha} - 2\eta\omega\dot{\alpha} + \omega^2\alpha = \mathbf{\Psi}^t\mathbf{F} + \mathbf{\Psi}^t\mathbf{K_a\phi_a} \tag{26}$$

and

$$\phi_s = \mathbf{K_{\phi_s\phi_s}^{-1}K_{\phi_s u}\Psi\alpha} - \mathbf{K_{\phi_s\phi_s}^{-1}K_{\phi_s\phi_a}\phi_a} \tag{27}$$

where ω is the diagonal matrix containing the eigenfrequencies. Note that a term of modal viscous damping has been added to take into account a small amount of natural damping without coupling the modes, η is the damping ratio.

4.2. State-space form

Eqs. (26) and (27) can be written in a state-space form :

$$\begin{cases} \dot{\mathbf{x}} = \mathbf{Ax} + \mathbf{B}\phi_a + \mathbf{f} \\ \mathbf{y} = \phi_s = \mathbf{Cx} \end{cases} \tag{28}$$

where $\mathbf{x}$ is the state-space vector defined as :

$$\mathbf{x} = \{\omega_n\alpha_n\dot{\alpha}_n\}_{(2N,1)}^t \tag{29}$$

The state matrix $\mathbf{A}$, the control output matrix $\mathbf{B}$, the observation matrix $\mathbf{C}$ and the load vector $\mathbf{f}$ are defined as:

$$\mathbf{A} = \begin{bmatrix} \mathbf{0} & \omega \\ -\omega & -2\eta\omega \end{bmatrix} \tag{30}$$

$$\mathbf{B} = \begin{bmatrix} \mathbf{0} \\ \mathbf{\Psi}^t\mathbf{K_a} \end{bmatrix} \tag{31}$$

$$\mathbf{C} = [\mathbf{K_{\phi_s\phi_s}^{-1}K_{\phi_s u}\Psi\omega^{-1}} \quad \mathbf{0}] \tag{32}$$

$$\mathbf{f} = \begin{bmatrix} \mathbf{0} \\ \mathbf{\Psi}^t\mathbf{F} \end{bmatrix} \tag{33}$$

where η is the diagonal matrix of the natural damping ratio.

4.3. Control law and observer

In order to actively control vibrations, a linear quadratic regulator (LQR) is used because its robustness ensures the system's stability even if actuators and sensors are not collocated [1]. Nevertheless, spillover effect due to the truncation of the modal basis must be considered. One solution is to optimize the location of sensors and actuators by taking into account the first residual modes into the optimization process [24].

Assuming that the state equation is controllable, the control law may be written as [38]:

$$\phi_a = -\kappa\mathbf{x} \tag{34}$$

where κ minimizes the cost function:

$$J_\phi = \frac{1}{2}\int_0^\infty \mathbf{x}^t\mathbf{Qx} + \phi_a^t\mathbf{R}\phi_a dt \tag{35}$$

$\mathbf{R}$ is a positive matrix and $\mathbf{Q}$is a positive semi-definite matrix. The optimal solution is:

$$\kappa = \mathbf{R^{-1}B^tP} \tag{36}$$

where $\mathbf{P}$ satisfies the Riccati equation:

$$\mathbf{A^tP} + \mathbf{PA} - \mathbf{PBR^{-1}B^tP} + \mathbf{Q} = 0 \tag{37}$$

The choice of $\mathbf{Q}$ and $\mathbf{R}$ is not easy. In the following applications, $\mathbf{Q}$ is chosen such that $\mathbf{x^tQx}$ represents the mechanical energy. The

components of **R** are chosen using the following statement: the maximal values of ϕ_a must be less than the maximal admissible values of the piezoelectric materials.

To be implemented, the optimal state control law needs knowledge of the state vector **x**. This knowledge is not complete since only the output voltages in **y** are observed. Assuming that the state system verifies the observability criteria, an estimation $\hat{\mathbf{x}}$ is computed using a Luenberger observer according to:

$$\dot{\hat{\mathbf{x}}} = \mathbf{A}\hat{\mathbf{x}} + \mathbf{B}\phi_a + \mathbf{L}(\mathbf{y}-\mathbf{C}\hat{\mathbf{x}}) \tag{38}$$

where **L** is the observance gain matrix. This matrix is chosen so that the real part of the eigenvalues of $\mathbf{A}-\mathbf{LC}$ are negative. Consequently, the control law applied to the FGPM actuators parts becomes:

$$\phi_a = -\kappa\hat{\mathbf{x}} \tag{39}$$

5. Numerical simulations

In this section, several studies are conducted in order to show the effect of some parameters (k, V_T, the electrodes' length and the electrodes' location) on both static and dynamic responses of FGPM beams described previously.

This section is divided in two parts. In static analysis, FGPM sensor sensitivity and actuator efficiency are investigated with k and V_T as variables. Then electrodes' length sensitivity is considered. In dynamic analysis, active vibration control for two configurations are performed.

The material properties and the beam geometry are given in Table 1 and Table 2, respectively.

5.1. Static study

In the following tests we consider a FGPM cantilever beam. Electrodes defining the actuator or sensor part are printed near the fixed end on top and bottom surfaces, and their length is $0.1m$.

5.1.1. FGPM sensor sensitivity
In order to show the FGPM sensor efficiency, a shearing force $F_s = 1N$ is applied at the free end of the beam.

Fig. 6 shows the effect of k and V_T on the sensor voltage output, which is shown to increase with these both parameters.

This can be explained by considering the FGPM sensor as a capacitor. In a capacitor, the voltage ϕ_g generated between its plates is given by:

$$\phi_g = \frac{de}{Y\,\epsilon} \tag{40}$$

where d is the distance between the capacitor's plates, e the piezoelectric constant, Y the Young modulus and ϵ the permittivity constant of capacitor's constitutive material.

In the FGPM structure, the distance d corresponds to the thickness of the insulating part: $d = h-h_c$. Thus, the sensor's output voltage behaviour follows this formula:

$$\phi_s \simeq \frac{(h-h_c)e_{31}}{Y\,\epsilon_{33}} \tag{41}$$

Table 1
Material properties.

Properties	Aluminium	PZT4
Young Modulus Y (GPa)	69	63
Poisson's ratio ν	0.3	0.3
Piezoelectric constant e_{31} (C/m^2)	0	-2.1
Dielectric constant ϵ_{33} (nF/m)	0	15
Density ρ (kg/m^3)	3960	7600

Table 2
Geometry data

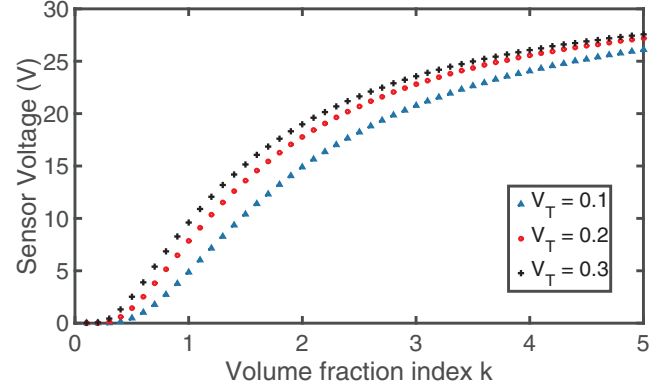| Properties	Value
Length L (m)	1
Thickness h (m)	0.01
Width b (m)	0.01

Fig. 6. FGPM sensor analysis: output sensor potential.

When the fraction index k increases, both $h-h_c$ and e_{31} increase and ϵ_{33} decreases. Furthermore, the percolation threshold V_T has only an effect on the quantity $h-h_c$, which increases when V_T increases. Therefore, the sensor voltage output when both the index k and V_T increase.

Fig. 6 shows also that the FGPM is inefficient if k is below a certain threshold, which may be denoted k_{lim}. In fact, when k tends to 0 the quantity $h-h_c$ tends also to 0. The present numerical simulations provide a value $k_{lim} = 0.4$ for all V_T.

Fig. 7 shows that the tip deflection increases with k and is independent of V_T. The beam's deflection is inversely proportional to its rigidity, which is mainly influenced by the Young modulus and barely by the electrical properties. When the fraction index k increases, the effective Young modulus decreases, as it tends towards the value of the PZT4 material which is lower than that of Aluminium. Note that , the percolation threshold does not influence the effective Young modulus and it has no influence on beam's deflection.

From the above considerations it can be concluded that the sensor efficiency is enhanced for high values of both, the k and the V_T parameters of the FGPM beam.

5.1.2. FGPM actuator efficiency
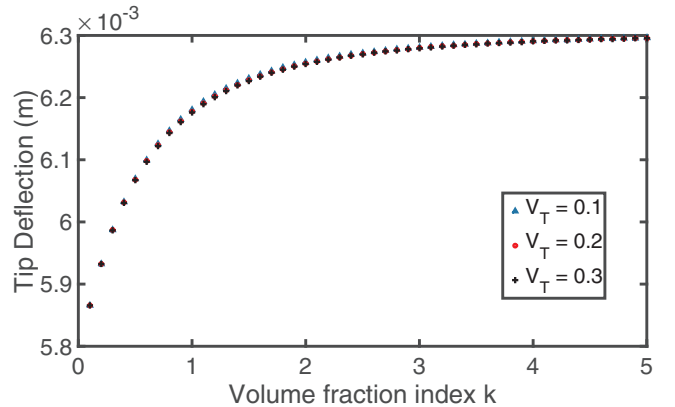We investigate the bending behaviour of FGPM cantilever beam
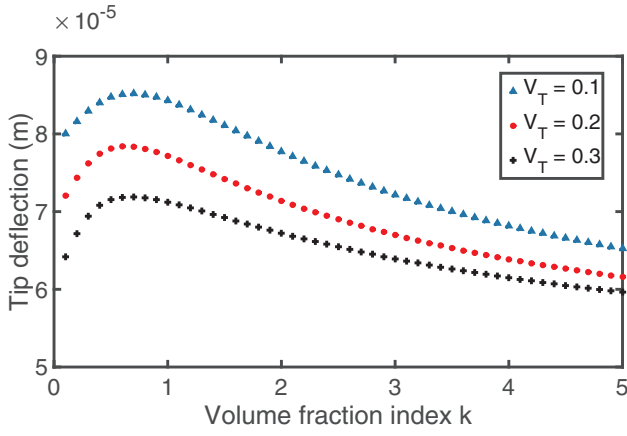

Fig. 7. FGPM sensor analysis: tip deflection.

Fig. 8. FGPM actuator analysis: tip deflection.

Fig. 9. FGPM sensor analysis: electrodes' length influence.

Fig. 10. FGPM actuator analysis: electrodes' length influence.

when an external voltage $\phi_a = 250\,\text{V}$ is applied to the electrodes.

For classical actuators, when only an external voltage ϕ_a is applied, the electrically induced bending deformation ε_a is primarily proportional to the piezoelectric coefficient e_{31} and ϕ_a. It is also inversely proportional to the insulating part's thickness $h-h_c$. Indeed it is well known that actuators are less efficient when they are thick. Thus, we have this relation of proportionality:

$$\varepsilon_a = \frac{\phi_a e_{31}}{h-h_c} \tag{42}$$

Fig. 8 shows the tip deflection of the FGPM beam as a function of the index k, for three values of V_T. The displacement does not change monotonically with k. This is similar to the typical 'non intermediate' behaviour of FGM under thermal loading that as been observed in previous works [39]. First, it increases until a maximal value for $k \in [0.4,0.7]$, then it decreases with k, mostly due to the increase of $h-h_c$. The percolation threshold V_T influences the quantity $h-h_c$, which increases when V_T increases; this explains the reduction of the actuator performances if V_T increases.

This investigation has thus demonstrated that an optimum actuator efficiency exists for $k \in [0.4,0.7]$ and the active deflection is higher for low value of V_T.

The above analysis of the actuator and sensor performances has shown that contradictory requirements are posed to the FGPM structure.

5.1.3. Electrodes' length study

A study on the length of the sensor and actuator is also performed. In both cases, the electrodes begin at the fixed end and their length varies from 10% to 100% of the beam length, with $k = 2$ and $V_c = 0.3$.

For the FGPM sensor case, the same load $F_s = 1N$ is applied at the free end for all configurations. The results reported in Fig. 9, show that the sensor potential output decreases with the electrode's length (Fig. 9), because the sensor potential is proportional to the strains, which decrease in the x-direction.

Considering the FGPM actuator case, the total electric charge is kept constant between all configurations in order to allow a direct comparison between them. Denoting L_0 and V_0 the length and potential of the reference electrode, the relation between the applied potential V_n and the electrode's length L_n of an different configuration is thus $V_n = \frac{V_0 L_n}{L_0}$. The numerical tests are computed by setting $V_0 = 250V$ and $L_0 = \frac{L}{10}$.

The results are given in Fig. 10. The tip deflection is shown to decrease with the electrode's length, which is explained by the fact despite the total resultant force excited by the actuator is constant for all configurations, its application point is progressively shifted away from the free end as the electrode's length increases.

This electrodes' length study shows that the efficiency of the FGPM actuation and sensing capabilities depends on the length of electrodes.
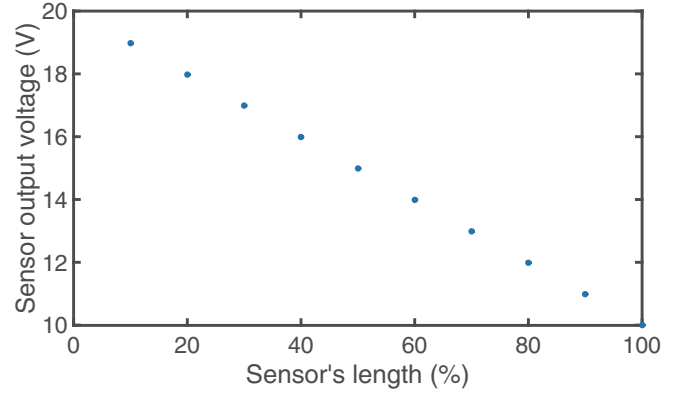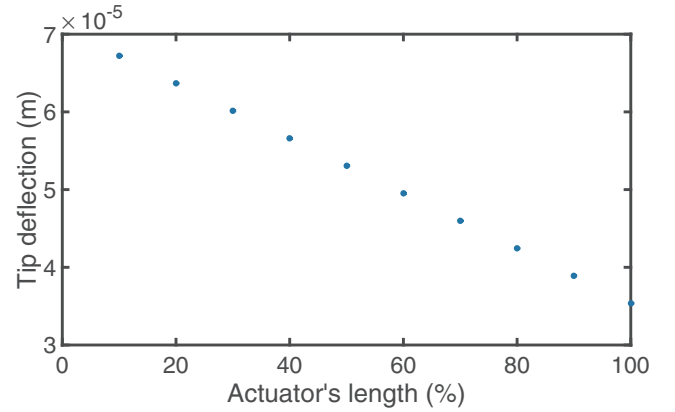
The electrodes' length should be chosen in agreement with the shape control or the sensor capability expected.

5.2. Dynamic study: active vibration control

In order to perform active vibration control, the maximal FGPM actuator's voltage input is chosen to 250 V and the observer's time response to 0.8 s. These two boundaries are respected with suitable **R** and **L** matrices respectively.

All dynamical simulations are lead over 10 s with a time step of $2e^{-5}$ s. The first four modes are used and the modal damping for each mode is taken equal to 5%.

5.2.1. FGPM cantilever beam: k and V_T parametric study

We consider a FGPM cantilever beam with actuator's electrodes located near the fixed end and sensor's electrodes located right after. Both electrodes are bounded at the top and bottom surfaces of the beam and have each a length of 0.1 L. Note that the sensor and actuator are not collocated. According to [23] this configuration is the optimal one for classical piezoelectric actuator and sensor on a cantilever beam, which ensures good observability and controllability of each eigenmodes.

Fig. 11 presents Bode diagrams for two values of k, in open loop (OL) and in closed loop (CL). They show clearly the gap between resonance frequencies for different values of k, and also show that active vibration is efficient since the first four peaks are attenuated.

The beam is subjected to a load $F_0 = 1N$ applied at $x = L$ during 10 periods of the first eigenfrequency.

In order to access the role of the index k on the active vibration control, three representative values of index k are considered in this test: the lowest $k = k_{lim}$ allowed for the sensor, $k = 1$ where the material distribution is linear, and a high index $k = 5$ where the FGPM is mostly
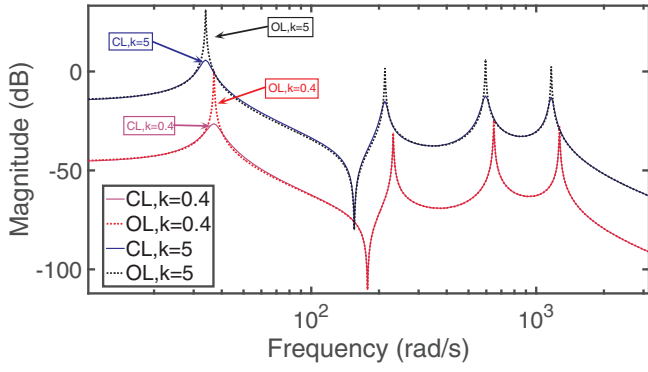
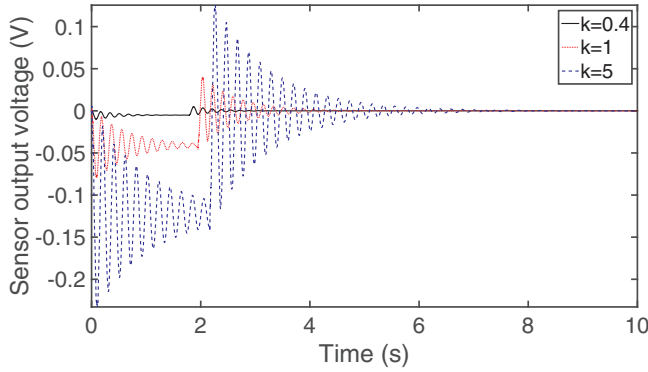**Fig. 11.** Bode diagram for $k = 0.4$ and $k = 5$ with $V_c = 0.3$.

Fig. 12. Step load k study: FGPM sensor output voltage for $V_c = 0.3$.

composed of $PZT4$.

Fig. 12 reports the sensor output voltages recorded over the simulation length of 10 s for the three values of k: the voltage is seen to increases for higher values of k, which confirms the result previously obtained for the static analysis. In these cases, the percolation threshold is fixed to $V_T = 0.3$.

Figs. 13 and 14 show the effect of k on the required FGPM actuator's input voltage and on the tip deflection, respectively. For open loop response, only structural damping attenuates the vibrations. For closed loop responses, the active control force is shown to annihilate the vibrations. The active control is efficient for all values of k. The best active control is achieved for $k = 0.4$: even if the FGPM sensor's output voltage is the lowest, the observer still ensures a good estimation of the structure's state.

To study the influence of V_T, k is fixed to 0.4. The FGPM sensor's output amplitude increases with V_T, in agreement with the static study (Fig. 15). For the lowest value of V_T, the sensor output voltage becomes very low. Note that such small values of output voltage should be
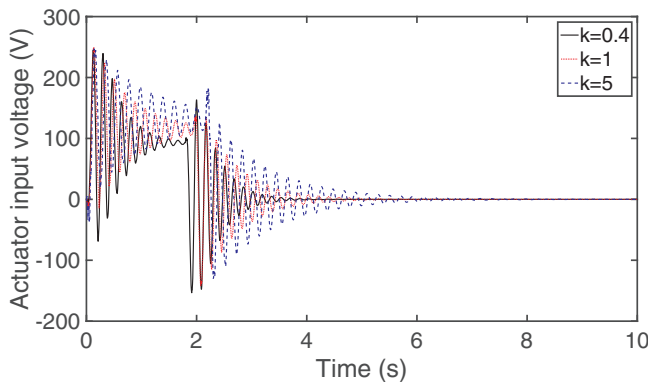

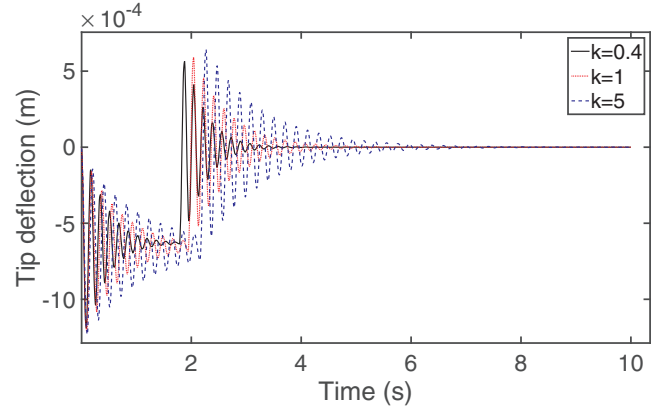**Fig. 13.** Step load k study: FGPM actuator input voltage for $V_c = 0.3$.

Fig. 14. Step load k study: Tip deflection for $V_c = 0.3$.
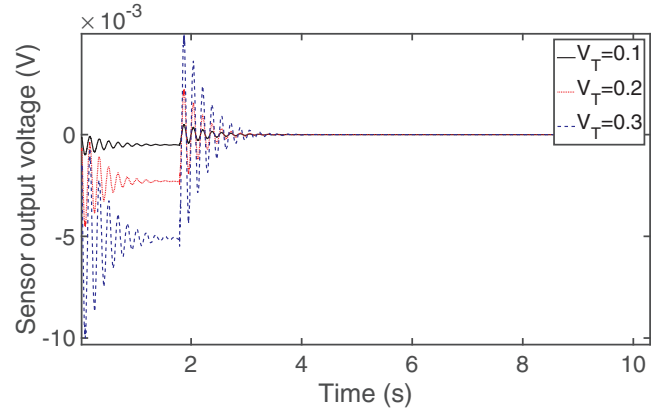

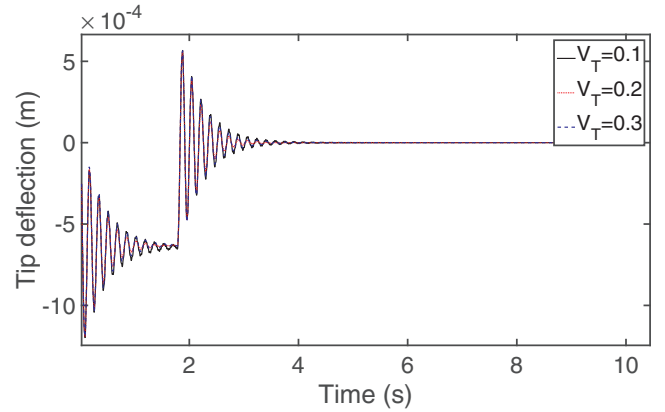**Fig. 15.** Step load V_T study: FGPM sensor output voltage for $k = 0.4$.

Fig. 16. Step load V_T study: Tip deflection for $k = 0.4$.

avoided because they could be interpreted as noise measurements. Fig. 16 and 17 show the tip deflection and FGPM actuator's input, respectively. Since V_T has nearly no influence on beam's rigidity the three curves in Fig. 16 are practically indistinguishable.

Between all studied configurations, the case $V_c = 0.2$ and $k = 0.4$ leads to the best performance. Other tests have been conducted on the cantilever FGPM beam, i.e., a release test and sinusoidal load test. These tests yield the same conclusions and are not reported here for the sake of brevity.

5.2.2. Simply supported FGPM beam: electrodes' location study

A simply supported FGPM beam is considered with collocated actuator and sensor electrodes. The length of the electrodes is fixed to 0.1 m and three locations are considered: with reference to Fig. 18, the
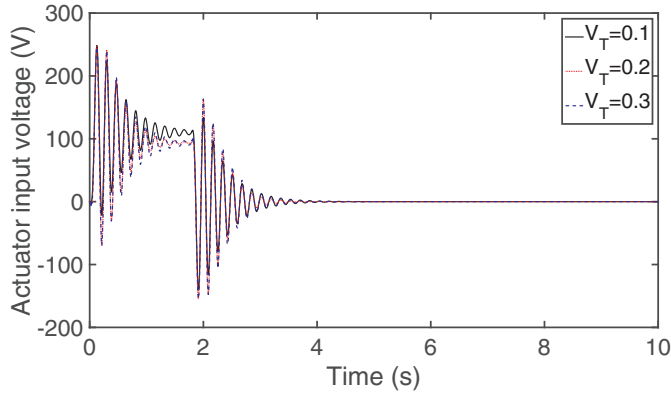
Fig. 17. Step load V_T study: FGPM actuator input voltage for $k = 0.4$.
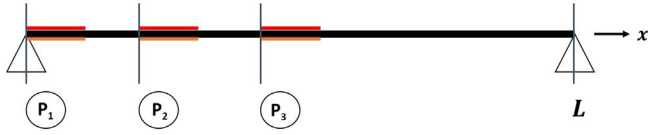

Fig. 18. Simply supported FGPM beam: electrodes' location.

left-most x coordinates of the electrode are $\{P_1, P_2, P_3\} = \{0, 0.225, 0.450\}$.

The most efficient values for k and V_T obtained previously are used, i.e. $k = 0.4$ and $V_c = 0.2$.

The beam is subjected to two different sinusoidal loads:

$$F_1(t) = \cos(0.8\omega_1 t) \qquad at \; x = \frac{L}{2}$$
$$F_2(t) = 10\cos(1.2\omega_2 t) \qquad at \; x = \frac{L}{4}$$

The first load F_1, activates predominantly the first mode, while F_2 the second one.

The different configurations are compared from the study of system's energy, which can be split into mechanical energy and electrical energy density, respectively given by:

$$E_m(t) = \{x(t)\}^t \{x(t)\} \tag{43}$$

$$E_{el}(t) = \{\phi^a(t)\}^t [\epsilon] \{\phi^a(t)\} \tag{44}$$

For the sake of reading, only the upper envelop of energies is plotted. Figs. 19 and 21 and Figs. 20 and 22 report respectively the evolution of the non dimensional mechanical energy and the non dimensional electrical energy density, during the simulation time ($10s$) for the F_1 and F_2 loading.

When the FGPM beam is subjected to the load F_1 all configurations can actively control the vibration of the beam, as the mechanical energy is lowered by the control system (Fig. 19). The most effective location is
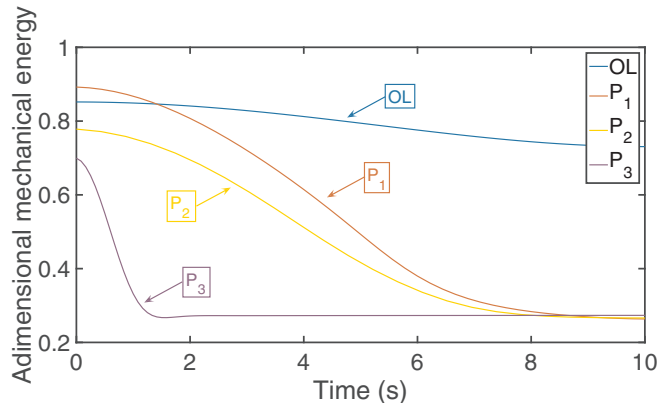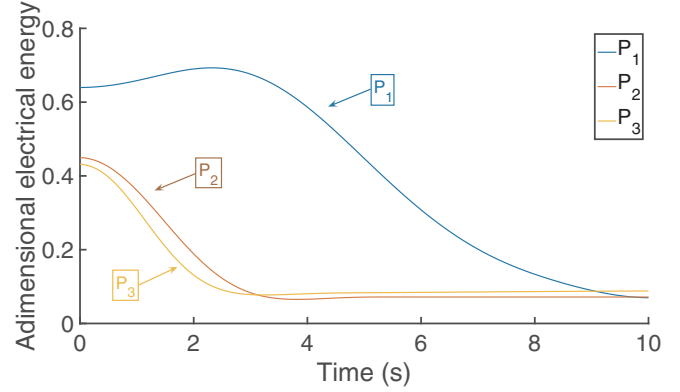

Fig. 20. Simply supported FGPM beam, F_1 load: electrical energy.
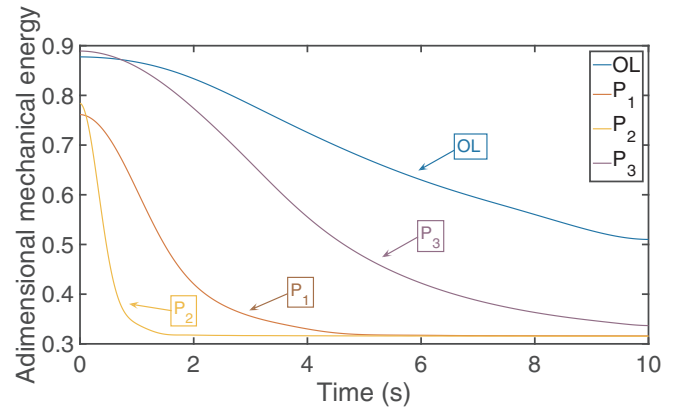

Fig. 21. Simply supported FGPM beam, F_2 load: mechanical energy.

P_3 as this location leads to the highest mechanical energy reduction, using the less input electrical energy (Fig. 20). The location P_2 is quite similar to P_3. Whereas P_1 is clearly less effective.

For the second loading that excites primarily the second mode, again all configurations perform active control vibration (Fig. 21). In this case, the most effective location is P_2. It is also the location which needs the less electrical energy in order to control vibration (see Fig. 22).

As expected, the optimal location of the electrodes depend on the predominant eigenmode of the dynamic response. A dedicated controller could be able to use one or more electrodes of the FGPM beam to perform efficient and stable active vibration control.
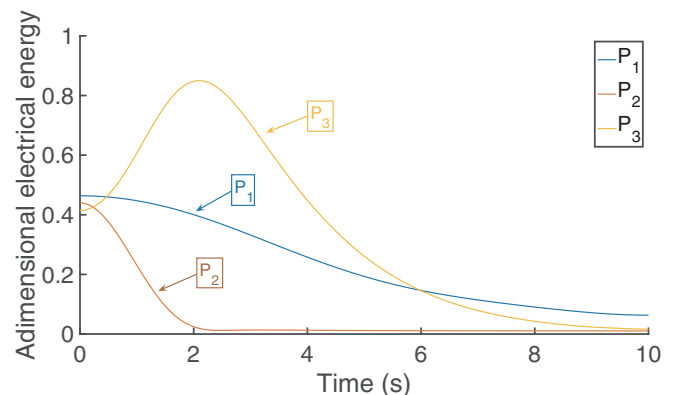

Fig. 19. Simply supported FGPM beam, F_1 load: mechanical energy.

Fig. 22. Simply supported FGPM beam, F_2 load: electrical energy.

6. Conclusion

Numerical static and dynamic studies have been carried out on a smart beam structure made out of a single FGPM layer. The mechanical and electrical properties of the PZT4-aluminium based FGPM are graded in the thickness according to a power law distribution, with the exception of the permittivity, which follows the Maxwell-Garnett law. The percolation phenomenon has been taken into account, which discerns insulating and conductive regions within the material.

A dedicated finite element has been implemented for this FGPM beam, based on linear piezoelectric theory, Timoshenko kinematics and a numerical layerwise approximation along the thickness for the electrical potential. The finite element is used to perform static analysis and to obtain the modal basis used for actively controlling the dynamic response of the beam. The FGPM beam is equipped with discrete electrodes in order to sense and actuate the vibrations. An efficient LQR control law with a state observer has been implemented and active control simulations have been achieved.

The simulations results show that the FGPM smart beam can be efficiently applied for static shape control as well as active vibration control. Parametric studies on the fraction index k and on the percolation threshold V_T shown that k has a huge influence on FGPM beam's sensing and actuation capabilities, whereas V_T plays a minor role. According to the studied cases, the sensing capability is optimised for high values of k, while the actuation capability is optimised for low values. This FGPM beam smart structure can perform active vibration control for a large range of values for k and shows its best performance when its actuation capability is optimised.

FGPM's actuation and sensing capabilities are also dependent on electrodes' dimensions and location.

In our future works, a sensitivity study about these geometrical parameters will be considered for FGPM plate. As the electrodes can be designed in any shapes and easily distributed all over the FGPM's surfaces, a well suited optimization method will be developed. Moreover, the multiplicity of electrodes will require the use of a novel control law defining the best set of electrodes to perform active vibration control in agreement with the external excitations.

References

[1] Preumont A. Vibration control of active structures: an introduction, vol. 179. Springer Science & Business Media; 2011.

[2] Pritchard J, Bowen C, Lowrie F. Multilayer actuators: review. Br Ceram Trans 2013;100(6):265–73.

[3] Mahamood RM, Akinlabi ET, Shukla M, Pityana S. Functionally graded material: an overview, Proceedings of the World Congress on Engineering, WCE 2012; 2012.

[4] Komeili A, Akbarzadeh AH, Doroushi A, Eslami MR. Static analysis of functionally graded piezoelectric beams under thermo-electro-mechanical loads. Adv Mech Eng 2011;3:153731.

[5] Lee H-J. Layerwise laminate analysis of functionally graded piezoelectric bimorph beams. J Intell Mater Syst Struct 2005;16(4):365–71.

[6] Nourmohammadi H, Behjat B. Design criteria for functionally graded piezoelectric plates under thermo-electro-mechanical loadings. J Intell Mater Syst Struct 2016;27(16):2249–60.

[7] Brischetto S, Carrera E. Refined 2d models for the analysis of functionally graded piezoelectric plates. J Intell Mater Syst Struct 2009;20(15):1783–97.

[8] Yang J, Xiang H. Thermo-electro-mechanical characteristics of functionally graded piezoelectric actuators. Smart Mater Struct 2007;16(3):784–97.

[9] Doroushi A, Eslami M, Komeili A. Vibration analysis and transient response of an fgpm beam under thermo-electro-mechanical loads using higher-order shear deformation theory. J Intell Mater Syst Struct 2011;22(3):231–43.

[10] Komijani M, Kiani Y, Esfahani S, Eslami M. Vibration of thermo-electrically post-buckled rectangular functionally graded piezoelectric beams. Compos Struct 2013;98:143–52.

[11] Parashar SK, Sharma P. Modal analysis of shear-induced flexural vibration of fgpm beam using generalized differential quadrature method. Compos Struct 2016;139:222–32.

[12] Behjat B, Salehi M, Armin A, Sadighi M, Abbasi M. Static and dynamic analysis of functionally graded piezoelectric plates under mechanical and electrical loading. Sci Iranica 2011;18(4):986–94.

[13] Bodaghi M, Damanpack A, Aghdam M, Shakeri M. Geometrically non-linear transient thermo-elastic response of fg beams integrated with a pair of fg piezoelectric sensors. Compos Struct 2014;107:48–59.

[14] Fakhari V, Ohadi A. Nonlinear vibration control of functionally graded plate with piezoelectric layers in thermal environment. J Vib Control 2011;17(3):449–69.

[15] Fu Y, Wang J, Mao Y. Nonlinear vibration and active control of functionally graded beams with piezoelectric sensors and actuators. J Intell Mater Syst Struct 2011;22(18):2093–102.

[16] Gharib A, Salehi M, Fazeli S. Deflection control of functionally graded material beams with bonded piezoelectric sensors and actuators. Mater Sci Eng: A 2008;498(1):110–4.

[17] Liew K, He X, Ng T, Sivashanker S. Active control of FGM plates subjected to a temperature gradient: modelling via finite element method based on FSDT. Int J Numer Meth Eng 2001;52(11):1253–71.

[18] Kargarnovin M, Najafizadeh M, Viliani N. Vibration control of a functionally graded material plate patched with piezoelectric actuators and sensors under a constant electric charge. Smart Mater Struct 2007;16(4):1252–9.

[19] Liew K, Sivashanker S, He X, Ng T. The modelling and design of smart structures using functionally graded materials and piezoelectrical sensor/actuator patches. Smart Mater Struct 2003;12(4):647–55.

[20] Mirzaeifar R, Bahai H, Shahab S. Active control of natural frequencies of FGM plates by piezoelectric sensor/actuator pairs. Smart Mater Struct 2008;17(4):045003.

[21] Narayanan S, Balamurugan V. Finite element modelling of piezolaminated smart structures for active vibration control with distributed sensors and actuators. J Sound Vib 2003;262(3):529–62.

[22] Sheng G, Wang X. Active control of functionally graded laminated cylindrical shells. Compos Struct 2009;90(4):448–57.

[23] Bruant I, Proslier L. Improved active control of a functionally graded material beam with piezoelectric patches. J Vib Control 2015;21(10):2059–80.

[24] Bruant I, Proslier L. Optimal location of piezoelectric actuators for active vibration control of thin axially functionally graded beams. Int J Mech Mater Des 2016;12(2):173–92.

[25] Bodaghi M, Damanpack A, Aghdam M, Shakeri M. Non-linear active control of FG beams in thermal environments subjected to blast loads with integrated FGP sensor/actuator layers. Compos Struct 2012;94(12):3612–23.

[26] Sharma A, Kumar A, Kumar R, Vaish R, Chauhan VS. Finite element analysis on active vibration control using lead zirconate titanate-pt-based functionally graded piezoelectric material. J Intell Mater Syst Struct 2016;27(4):490–9.

[27] Susheel C, Kumar R, Chauhan VS. Active shape and vibration control of functionally graded thin plate using functionally graded piezoelectric material. J Intell Mater Syst Struct.

[28] Chỳlek P, Srivastava V. Dielectric constant of a composite inhomogeneous medium. Phys Rev B 1983;27(8):5098.

[29] Pecharromán C, Moya JS. Experimental evidence of a giant capacitance in insulator-conductor composites at the percolation threshold. Adv Mater 2000;12(4):294–7.

[30] Reddy JN. An introduction to the finite element method, vol. 2. McGraw-Hill New York; 1993.

[31] Li J-F, Takagi K, Terakubo N, Watanabe R. Electrical and mechanical properties of piezoelectric ceramic/metal composites in the Pb(Zr, Ti)O3/Pt system. Appl Phys Lett 2001;79(15):2441–3.

[32] Takagi K, Li J-F, Yokoyama S, Watanabe R, Almajid A, Taya M. Design and fabrication of functionally graded pzt/pt piezoelectric bimorph actuator. Sci Technol Adv Mater 2002;3(2):217–24.

[33] Orlowska S. Conception et prédiction des caractéristiques diélectriques des matériaux composites à deux et trois phases par la modélisation et la validation expérimentale [Ph.D. thesis]. Ecole Centrale de Lyon; 2003.

[34] Polit O, Bruant I. Electric potential approximations for an eight node plate finite element. Comput Struct 2006;84(22):1480–93.

[35] Osmont D, Pablo F. Use of classical plate finite elements for the analysis of electroactive composite plates: theoretical aspects. J Intell Mater Syst Struct 2009;20(15):1845–60.

[36] Benjeddou A, Belouettar S, Topping B, Montero G, Montenegro R. On the evaluation and application of the modal properties of piezoelectric adaptive structures, Innovation in Computational Structures Technology. Stirlingshire: Saxe-Coburg Publications; 2006. p. 287–302.

[37] Burl JB. Linear optimal control: H (2) and H (Infinity) methods. Addison-Wesley Longman Publishing Co., Inc; 1998.

[38] Kailath T. Linear Systems vol. 156. NJ: Prentice-Hall Englewood Cliffs; 1980.

[39] Reddy J. Analysis of functionally graded plates. Int J Numer Meth Eng 2000;47(1–3):663–84.